www.acsnano.org

# Machine Learning-Assisted Near-Infrared Spectral Fingerprinting for Macrophage Phenotyping

Aceer Nadeem, Sarah Lyons, Aidan Kindopp, Amanda Jamieson, and Daniel Roxbury\*



Downloaded via Daniel Roxbury on August 16, 2024 at 23:46:19 (UTC). See https://pubs.acs.org/sharingguidelines for options on how to legitimately share published articles.

Cite This: https://doi.org/10.1021/acsnano.4c03387



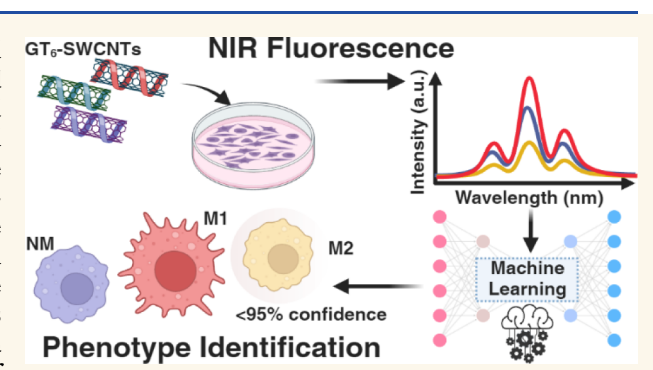
**ACCESS** 

III Metrics & More

Article Recommendations

Supporting Information

ABSTRACT: Spectral fingerprinting has emerged as a powerful tool that is adept at identifying chemical compounds and deciphering complex interactions within cells and engineered nanomaterials. Using near-infrared (NIR) fluorescence spectral fingerprinting coupled with machine learning techniques, we uncover complex interactions between DNA-functionalized single-walled carbon nanotubes (DNA-SWCNTs) and live macrophage cells, enabling in situ phenotype discrimination. Utilizing Raman microscopy, we showcase statistically higher DNA-SWCNT uptake and a significantly lower defect ratio in M1 macrophages compared to M2 and naive phenotypes. NIR fluorescence data also indicate that distinctive intraendosomal environments of



these cell types give rise to significant differences in many optical features, such as emission peak intensities, center wavelengths, and peak intensity ratios. Such features serve as distinctive markers for identifying different macrophage phenotypes. We further use a support vector machine (SVM) model trained on SWCNT fluorescence data to identify M1 and M2 macrophages, achieving an impressive accuracy of >95%. Finally, we observe that the stability of DNA-SWCNT complexes, influenced by DNA sequence length, is a crucial consideration for applications, such as cell phenotyping or mapping intraendosomal microenvironments using AI techniques. Our findings suggest that shorter DNA-sequences like  $GT_6$  give rise to more improved model accuracy (>87%) due to increased active interactions of SWCNTs with biomolecules in the endosomal microenvironment. Implications of this research extend to the development of nanomaterial-based platforms for cellular identification, holding promise for potential applications in real time monitoring of *in vivo* cellular differentiation.

KEYWORDS: spectral fingerprinting, nanomaterials, machine learning, confocal Raman microscopy, near-infrared fluorescence, intracellular processing, single-walled carbon nanotubes

Biosensing is a rapidly emerging sector of the biomedical engineering field, specifically in human healthcare due to the noninvasive nature and tunable specificity of recent sensors. Typical examples of biosensors, include immunosensors, DNA biosensors, enzyme-based biosensors, thermal and piezoelectric biosensors, and optical biosensors, which utilize affinity toward antigens, chemical interactions, thermal fluctuations, affinity interactions, and fluorescence, respectively, to pinpoint the presence or concentration change of a specific biological marker. Certain optical biosensors are of particular interest as they implement a light source to probe changes within cellular environments that can cause shifts in fluorescence wavelength, intensity, and/or spectral bandwidth, which can be attributed to distinct cellular microenvironments. 8–11

Single-walled carbon nanotubes (SWCNTs) have been successfully utilized as *in vitro* optical biosensors due to their

intrinsic fluorescence and photostability. <sup>12,13</sup> Moreover, the fluorescence of SWCNTs resides within the near-infrared (NIR) spectrum, a region which proves useful in biological imaging applications due to limited tissue absorbance, scattering, and autofluorescence. <sup>14–16</sup> SWCNTs can be noncovalently functionalized with biocompatible polymers and biomolecules to increase environmental biocompatibility. <sup>17</sup> Specifically, there has been success with different types of amphiphilic functionalization, such as single-stranded DNA

Received: March 11, 2024 Revised: July 29, 2024 Accepted: August 1, 2024



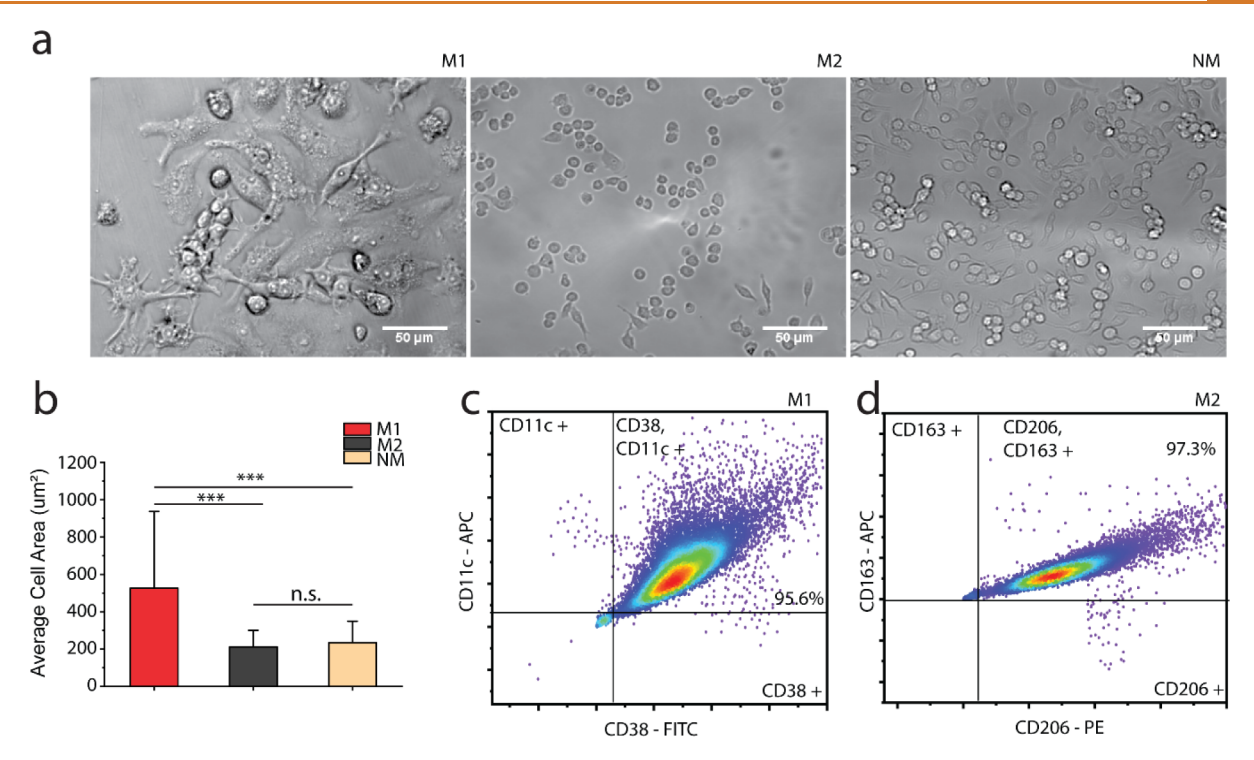


Figure 1. Cell Characterization. (a) Transmitted light images of M1, M2, and naive macrophages, with scale bar of 50  $\mu$ m. (b) Bar graph for average cell area, bars represent the average, and whiskers represent mean  $\pm$  s.d. for each condition ( $n \ge 500$  cells per condition). Two-sample t test hypothesis testing analysis was performed between different samples (\*\*\*p < 0.001). Fluorescent surface marker dependent flow cytometry density plot for (c) M1 type macrophages and (d) M2 type macrophages, for each condition  $n \ge 5 \times 10^6$  cells mL<sup>-1</sup>.

(ssDNA) and polyethylene glycol (PEG)-lipid conjugate wrappings. <sup>18–20</sup> Through appropriate biocompatible functionalization, SWCNTs can be effectively internalized into mammalian cells via energy dependent endocytosis and phagocytosis, where they then enter the endosomal pathway and eventually localize within the lysosomes. <sup>21,22</sup> The amphiphilic wrappings of SWCNTs prove to be biocompatible as various studies have shown endocytosis and endosomal escape from different cell lines with negligible introduced toxicities. <sup>23,24</sup> We have previously shown that DNA sequence length plays a significant role in determining endocytosis and retention durations of DNA-functionalized single-walled carbon nanotubes (SWCNTs) within mammalian cells. <sup>19</sup>

Macrophages are immune cells of high interest in the field of biomedicine due to their implication in immune responses, inflammation regulation, and tissue repair. Macrophages play a crucial role in various biomedical contexts, such as host defense against pathogens, clearance of cellular debris, modulation of immune response, and wound healing.<sup>25</sup> Their versatility makes them a key player in understanding and addressing diseases including infections, autoimmune disorders, and cancer. Macrophages are capable of polarizing and differentiating from monocytes and a naive state into, broadly characterizing, either pro-inflammatory M1 phenotypes or prohealing M2 phenotypes. 26,27 These phenotypical changes are induced by signaling molecules and cytokines in the local cellular microenvironment. 28,29 The inflammatory responses performed by M1 macrophages are dominated by toll-like receptor (TLR) and interferon signaling and can be polarized in vitro with interferon gamma (IFN-γ), tumor necrosis factor alpha (TNF- $\alpha$ ), and lipopolysaccharide (LPS). <sup>30,31</sup> In contrast, M2 macrophages are found in the proliferation and remodeling phases of wound healing, secreting cytokines to actively

promote repair and recruit various cell types to clear cellular debris. <sup>32,33</sup> Typical cytokines implicated in the differentiation of M2 macrophages are interleukin-4 (IL-4) and interleukin-10 (IL-10). <sup>34,35</sup>

The shift from inflammation to proliferation represents a pivotal stage in the wound healing process. An imbalance in the macrophage phenotype environment and the inability to transition between M1 and M2 states can lead to ulcers and chronic wounds. 32,36 The wound healing process is similar to the human body's reaction to diseases, such as cancers. In certain cancers, such as colorectal cancer, tumor cells will utilize macrophage anti-inflammatory characteristics to promote tumor growth, thus progressing the spread of cancer.<sup>37</sup> Due to the vast differences between macrophage polarization states, there must be tight control of differentiation to avoid prolonged periods of inflammation. However, in the presence of chronic inflammation, imbalances of M1 and M2 phenotypes are observed and ultimately trigger changes in macrophage behavior.<sup>38</sup> By quantifying and preventing changes in macrophage polarization states, there is potential for a decrease in disease progression.<sup>39</sup>

To identify M1 and M2 macrophage phenotypes and quantify any potential imbalance, in both wound healing and other affected disease, flow cytometry, 40 surface marker analysis, 41 and visual morphological confirmation via optical microscopy are frequently employed. 42,43 Flow cytometry serves as a method that can rapidly differentiate different cells in a sample with high-throughput analysis. However, this method is not well adapted to identify different subsets of macrophage phenotypes as it requires a diverse array of surface markers and dyes, which become prohibitively expensive. 44 Moreover, issues in data collection can arise when samples have been exposed to fibrosis or other pathological changes,

which is common in wound sites. 45 Other limitations of flow cytometry, include breakdown of antibody tandem dyes, which effects variability in emission spectra, and thus, reliability as well as other analytical and interpretation pitfalls. 46 High equipment purchasing and maintenance costs are also a disadvantage when it comes to flow cytometry. The visual analysis of macrophage phenotypes via optical microscopy and immunofluorescence imaging can be useful in identifying M1 and M2 macrophages but becomes less reliable when comparting naive macrophages to M2 due to their similar morphologies. 47 Consequently, immunofluorescence microscopy has its own limitations like nonspecific binding. 48 Another limitation is the photobleaching of fluorochromes and fluorescent dyes being used. 49 Furthermore, the technique can be used only with fixed cells.

Morphological identification of samples through machine learning on cell shape and size, has been proven to predict M1 or M2 macrophages with an accuracy of 90%, 45 however, the identification of specific subtypes of cells within a diseased and heterogeneous sampling would be better served by a more robust method for classification as this method uses fluorescence dyes, which have their own limitations as discussed above. 48,49 Other label-free strategies of phenotype classification using autofluorescence and machine learning have also been employed, but they have only been able to achieve an accuracy of 75.8%, 50 as opposed to our robust method that can easily give an accuracy of 95% and can also easily be translated to a quick assay based detection method. In a previous study, we have shown that DNA-SWCNTs can be used to map intracellular processes based on modulations in their Raman spectra.<sup>51</sup> These differences induced throughout a single cell could be attributed to changes in the local environment of the SWCNTs, such as pH, salt concentration, or protein interactions. Here, utilizing NIR fluorescence data of SWCNTs within macrophages of varying phenotypes coupled with machine learning, we show that a similar spectral fingerprinting method can be developed to accurately identify live M1, M2, and naive macrophages. We find that DNA-SWCNTs are rapidly internalized into all macrophage phenotypes with M1 demonstrating the highest rate of uptake. Once inside, we observe interesting trends in the Raman spectra of the SWCNTs as well as a DNA-sequence specific modulation in NIR fluorescence. We uncover that SWCNTs dispersed with a short DNA sequence (i.e., GT<sub>6</sub>-SWCNTs) are able to undergo the largest degree of SWCNT chirality-dependent modulations in NIR fluorescence, enabling the highest accuracy of in vitro discrimination between macrophage phenotypes. The presented SWCNT spectral fingerprinting coupled with machine learning method is versatile and can be applied to other livecell discrimination analyses.

## **RESULTS AND DISCUSSION**

A model mammalian macrophage cell line (RAW 264.7 murine macrophages) was employed to investigate characteristic differences between naive (nonpolarized, "NM"), M1, and M2 macrophage phenotypes. Cell-type specific cytokines were added to NM cells to artificially stimulate them into differentially activated phenotypes M1 and M2. Figure 1a represents transmitted light images of each macrophage phenotype captured by bright field microscopy. Upon closer examination, noticeable differences in size (Figure S1) and morphology are evident (Figure S2). M2 displays a nearly round and circular morphology, like that of naive macrophages,

whereas M1 is larger in size, as well as lacking a well-defined shape. These distinct features offer visual confirmation that we have different species of macrophages. Figure 1b shows a statistical bar graph highlighting the significant difference in cell area and size between the three cell species; this area and sizes were determined using image analysis as detailed in Figure S3. Where M1 exhibits the largest average cell area measuring approximately 520  $\mu \rm m^2$ , M2 and NM are observed to be considerably smaller in size with an average area of 200  $\mu \rm m^2$  (61% smaller) for M2 and 240  $\mu \rm m^2$  (56% smaller) for naive macrophages.

Following a 24-hour cytokine dose, fluorescence-activated cell sorting flow cytometry (FACS) was conducted to further validate the macrophage phenotypes. In Figure 1c,d, fluorescent marker-specific cell density plots are presented, specifically gated to illustrate the population of M1 and M2 in the sample. Analysis of both scatter plots reveals that after the 24-hour cytokine dose, 95.6% of the cells in the sample exhibit M1 phenotype, while 97.3% display M2 macrophage phenotype. Figures S4 and S5 show how cell populations were first identified using forward and side scatter, followed by doublet cell exclusion using forward scatter height and area. Naive macrophages were used as a control in flow experiments as an initial reference to establish gating strategies.

It is imperative to recognize and address the inherent error in the data moving forward. This margin of error stems from challenges in achieving 100% polarization of cells, which is confirmed by our FACS results. This acknowledgment underscores the importance of exercising caution and precision in the interpretation of the results. It highlights the necessity for a thorough understanding of the limitations inherent in the current methodology employed in this study and the advantage of using a machine learning model to accurately predict phenotypes.

After confirming the degree of macrophage polarization, we next investigated the uptake of DNA-SWCNTs into the cells via confocal Raman microscopy. Macrophage cells that had been prepolarized for 24 h were treated with 1 mg  $L^{-1}$  of  $GT_{6}$ SWCNTs for 30 min, followed by a thorough washing with 1× phosphate-buffered saline (PBS), and subsequent incubation in fresh media for an additional 30 min. After this incubation period, the cells were fixed and immersed in PBS for confocal Raman microscopy. Transmitted light and confocal Raman images were captured from individual cells at a magnification of 100×, aiming to analyze characteristic SWCNT Raman features, such as the G-band (Figure 2a). The G-band, measured at 1585 cm<sup>-1</sup>, <sup>19</sup>, <sup>52</sup> exhibits a linear correlation with SWCNT concentration (Figure S6a), while the D-band (Figure S6b) (1350 cm<sup>-1</sup>)<sup>53</sup> to G-band ratio is indicative of the number of defects present on the SWCNT structure.<sup>54</sup> Figure 2b represents the average integrated intensity of the Gband per region of interest (ROI). Here, an ROI defines a particular cell containing SWCNTs. The average integrated Gband intensity per ROI was found to be highest for M1 (42 counts), followed by M2 (23 counts), and then NM (13 counts). Figure S7 shows the full graphical representation of these cells.

A statistical representation of the defect ratio  $(I_{\rm D}/I_{\rm G})$  for DNA-SWCNTs within all the macrophage phenotypes is presented in Figure 2c. The data reveal that the defect ratio in M1 macrophages is significantly lower compared to the M2 and NM cells, and that there is no statistically significant difference between M2 and NM. A closer look at these

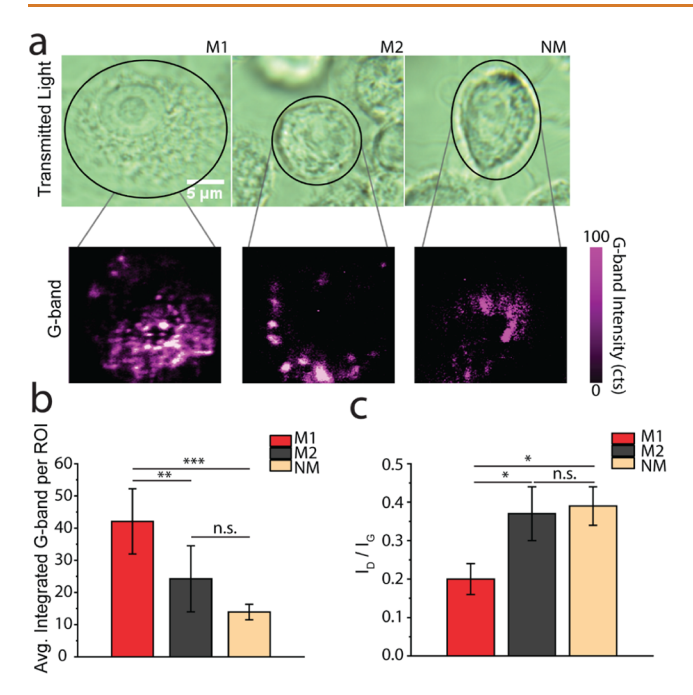


Figure 2. Raman microscopy characterization of cells containing DNA-SWCNTs. (a) Transmitted light images and magnified Raman G-band images separated by cell phenotype. The scale bar on images is  $5 \, \mu \text{m}$ . (b) Average integrated G-band intensity per ROI. (c) D-band to G-band ratio showing clear differences in all cell phenotypes. Bars represent the average and whiskers represent mean  $\pm$  s.d. for each condition ( $n \geq 4$  cells per condition). A two-sample t test hypothesis testing analysis was performed between different samples and between different time points. (\*\*\*p < 0.001, \*\*p < 0.01, and \*p < 0.05).

observations suggests some selectivity in defective SWCNT uptake in the M2 and NM cells. Our previous studies have shown that macrophages can induce defects and selectively internalize defective SWCNTs. This supports our hypothesis that M2 and NM cells selectively internalize SWCNTs with more defects, thus having a higher defect ratio. These results underline the intricate relationship between nanotube interaction and the internal cellular makeup, providing valuable insights into the nanomaterial cell dynamics.

Near-infrared hyperspectral fluorescence microscopy<sup>15</sup> was performed on macrophage cells with internalized DNA-SWCNTs. All the data was acquired as a function of DNA length. Three oligonucleotide sequences (GT<sub>6</sub>, GT<sub>15</sub>, and GT<sub>30</sub>) were employed in this study. DNA sequences composed of guanine—thymine (GT) repeat units were chosen for their widespread and comprehensive study in literature.<sup>19</sup> Detailed Analysis of GT<sub>6</sub>, GT<sub>15</sub>, and GT<sub>30</sub>-SWCNTs can be found in Figure S8–14.

Each cell type (M1, M2, or NM) was incubated with 1 mg L<sup>-1</sup> of GT<sub>G</sub>-SWCNTs for 30 min, followed by a wash with PBS, and subsequent incubation in fresh media for 30 min, 6 h, or 24 h before hyperspectral imaging. Throughout this period, changes in peak intensity and center wavelength were observed for four distinct emission bands in the NIR spectrum for each macrophage phenotype. A two-dimensional excitation/emission photoluminescence plot in Figure S15 shows all of the chiralities present in our DNA-SWCNT sample. From shortest to longest wavelength, we used the four strongest emission bands, which are dominated by the (10,2), (9,4), (8,6), and (8,7)-SWCNT chiralities.<sup>51</sup> Figure 3a shows the transmitted

light and NIR images for all three macrophage phenotypes, M1, M2, and NM 6 h post DNA-SWCNT dose. Visual differences in intensity can easily be observed, with M1 being brighter than M2 and NM. Figure 3b shows the average broadband intensity for each cell type normalized by their respective areas. In principle, the NIR broadband intensity of M1 macrophages should ideally be significantly higher than that of M2 and naive macrophages due to higher uptake in M1, as indicated by a higher G-band. However, it is important to note that the average cell size of M1 macrophages, as discussed earlier in Figure 1b, is significantly larger in comparison to that of M2 and NM cells. When divided by the projected cell area in two-dimensions, this normalized broadband intensity turns out to be the smallest. The average area-normalized broadband intensity for M1 cells was observed to be a striking 72% less than M2. Furthermore, the average intensity for NM cells was observed to be approximately 45% less than that of M2 type macrophages. Nevertheless, it is crucial to emphasize that, whether normalized by cell area or not, the broadband intensity differs significantly across all cell phenotypes. This distinction suggests that the broadband intensity can serve as an identifiable feature for distinguishing cell phenotypes. Figure 3c shows averaged spectral data at the 6 h time point, which reveals distinct differences and variations in normalized intensities and peak center wavelengths among M1, M2, and NM cells. Similar apparent trends and modulation in the center wavelengths and peak intensities can be observed between these cell phenotypes throughout all time points (Figure S16–20). To study identifiable spectral differences between M1, M2, and NM cells, we probed various NIR fluorescence parameters in more detail. Figure 3d is a statistical comparison of the peak intensity ratios for bands 1 and 2. Statistically significant differences between all cell phenotypes is observed.

We next fitted the average NIR spectra to Gaussian curves to extract peak intensity and center-wavelength information for each of the identified SWCNT bands (Figure S21). The center-wavelength information is shown for the 6 h time point in Figure 3e, where it is apparent that both M1 and M2 type macrophages exhibit center wavelength modulations when compared to NM. M1 macrophages exhibited a 4 nm red-shift in band 1 center wavelength when compared to NM cells, whereas M2 macrophages exhibited a 3 nm red-shift. It is important to note that although the wavelength difference between M1 and M2 cells is just 1 nm, it is still statistically significant and thus can be used as one of the identifiable features in NIR macrophage phenotyping. Figure S22 shows a list of different NIR features that were evaluated and used in machine learning.

We speculate that the observed changes in intensity and center wavelength over 24 h, as well as the differences in peak intensities and center wavelengths of different chiral species, are likely attributed to variations in the lysosomal environment of these three distinct cell phenotypes.

Previous work in the literature has demonstrated that DNA-SWCNTs undergo internalization into cells through energy dependent endosomal uptake and endolysosomal processing. <sup>19</sup>, <sup>22</sup> It is also a known fact that the endosomal environment for different cell phenotypes, such as M1 and M2 macrophages, can significantly differ. <sup>56</sup> For instance, M1 macrophages exhibit upregulation of NOX2, iNOS, SYNCRIP, TRAF6, AP-1, and certain cathepsin species, while M2 macrophages show downregulation of NOX2, iNOS, SYNCRIP, and upregulation

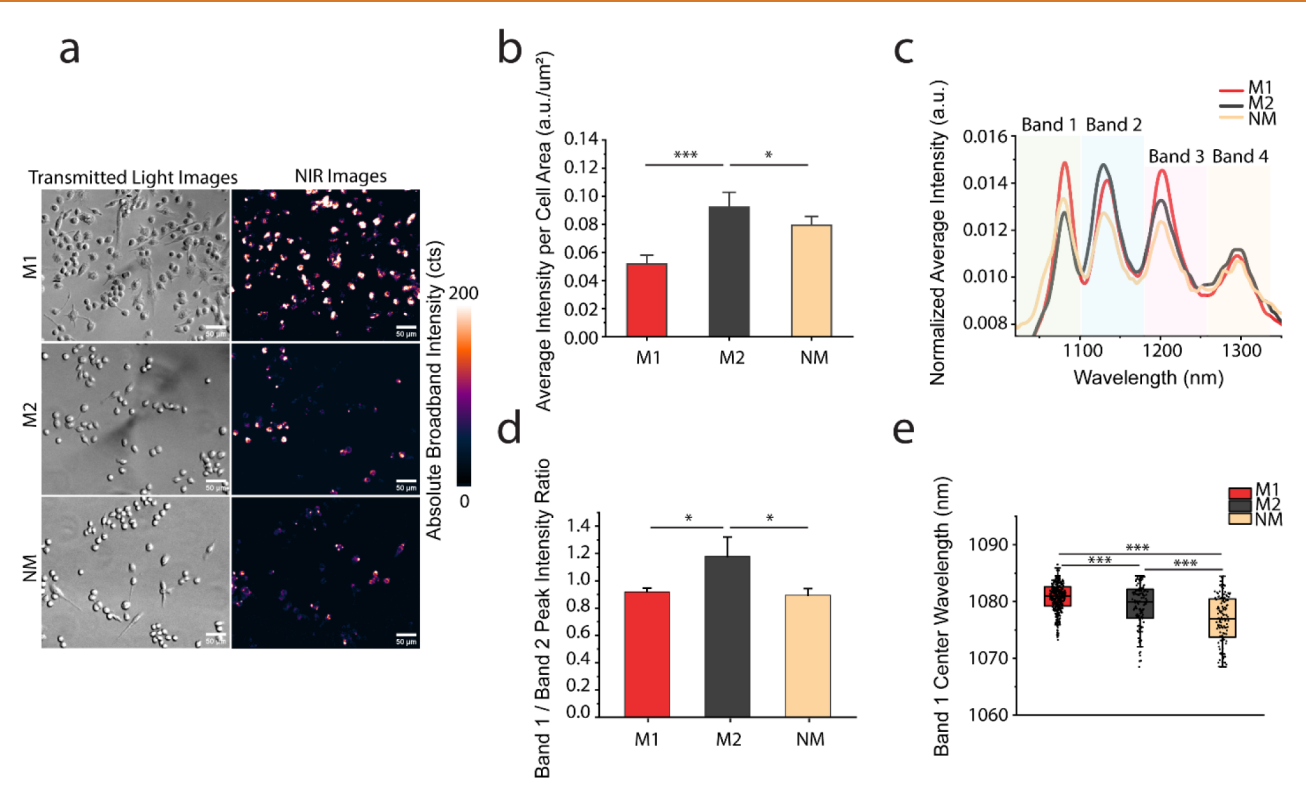


Figure 3. NIR fluorescence hyperspectral microscopy and identification of spectral features for  $GT_6$ -SWCNTs in various macrophage phenotypes 6 h after internalization. (a) Transmitted light and NIR fluorescence images (900–1600 nm) for all cell types M1, M2, and NM. (b) Bar graph showing average broadband intensity per cell area for all cell phenotypes. Bars represent the average and whiskers represent the mean  $\pm$  s.d. for each condition ( $n \ge 300$  cells per condition). A two-sample t test hypothesis testing analysis was performed between different samples and between different time points (\*\*\*p < 0.001, and \*p < 0.05). (c) Average NIR spectrum for  $GT_6$ -SWCNTs within each cell phenotype. (d) Bar graph showing a comparison of band peak intensity ratios for all phenotypes. Bars represent the average and whiskers represent mean  $\pm$  s.d. for each condition ( $n \ge 300$  cells per condition). A two-sample t test hypothesis testing analysis was performed between different samples and between different time points (\*p < 0.05). (e) Box and whisker diagram for band 1 center wavelength. Minimum of  $p \ge 300$  cells per condition were used. Boxes represent 25–75% of the data, horizontal lines represent medians, and whiskers represent mean  $p \ge 3.00$  cells per condition were used. Boxes represent 25–75% of the data, horizontal lines represent medians, and whiskers represent mean  $p \ge 3.00$  cells per condition were used. Boxes represent 25–75% of the data, horizontal lines represent medians, and whiskers represent mean  $p \ge 3.00$  cells per condition were used. Boxes represent 25–75% of the data, horizontal lines represent medians, and whiskers represent mean  $p \ge 3.00$  cells per condition were used. Boxes represent 25–75% of the data, horizontal lines represent medians, and whiskers represent mean  $p \ge 3.00$  cells per condition were used. Boxes represent 25–75% of the data, horizontal lines represent medians, and whiskers represent mean  $p \ge 3.00$  cells per condition whiskers represent mean  $p \ge 3.00$  cells per c

of arginase, EGR2, SOD 1, and superoxide dismutase.<sup>57–59</sup> The significant differences in the intra-endosomal environment of these cells contribute to a complicated interplay between SWCNTs and cellular biomolecules. This interplay leads to preferential binding of specific analytes to different SWCNT chiral species, thus influencing the SWCNT spectrum.

To confirm this hypothesis, we performed solution phase experiments to recapitulate the intracellular environments. Figure 4a shows the response of GT<sub>6</sub>-SWCNTs to physiologically relevant concentrations of 10 ng mL<sup>-1</sup> deoxyribonuclease II (DNase II), activating protein-1 (AP-1), and a mixture of both. DNase-II and AP-1 were selected as model biomolecules from the lysosomal environment of various macrophages due to their pH dependence and phenotype-specific up or down regulation.<sup>58</sup> Similar to the differential phenotypic response as shown in Figure 3, all the biomolecules exhibit slight changes in peak intensity and band specific center wavelength, which significantly differ from the GT<sub>6</sub>-SWCNT control sample. Notably, the individual biomolecule responses also significantly differ from the combined biomolecule response when carefully examining all NIR spectra. It is also important to note that like intracellular NIR features in Figure 3 similar observations in center wavelength red-shifting and intensity changes are observed for the SWCNT bands between control, DNase-II, and AP-1 samples. Interestingly, the protein-induced spectral modulations are time-dependent (Figure 4c). Major shifts in SWCNT center wavelengths and peak intensities were observed for AP-1 solutions at time points of 1 or 6 h after mixing. Similar time-dependent spectral modulations were observed for DNase-II and the biomolecule mixture, as shown in Figure S23. These differences in SWCNT sensor response over time, specifically peak shifting and broadening, can also be attributed to protein-induced aggregation within the samples. The differential response of the DNA-SWNCTs under varying pH conditions is shown in Figure 4b. Finally, Figure 4d illustrates the variations in the peak intensity ratio between bands 1 and 2 across all model biomolecules, as depicted by the bar graph.

These solution phase experiments provide supporting evidence for the hypothesis that differences in the NIR spectrum of DNA-SWCNTs can indeed be caused by changes in the varying endolysosomal environment within distinct macrophage phenotypes.

The array of changes observed in the DNA-SWCNT spectra across different cell phenotypes and over time reflects the complex and dynamic nature of nanomaterial—cell interactions within distinct endolysosomal environments. This insight into the intricate molecular interactions can be used as an effective tool to differentiate between cell phenotypes. Utilizing all the NIR fluorescence features that exhibited significant differences between M1, M2, and NM cells, a machine learning (ML) model was developed for the identification and quantification

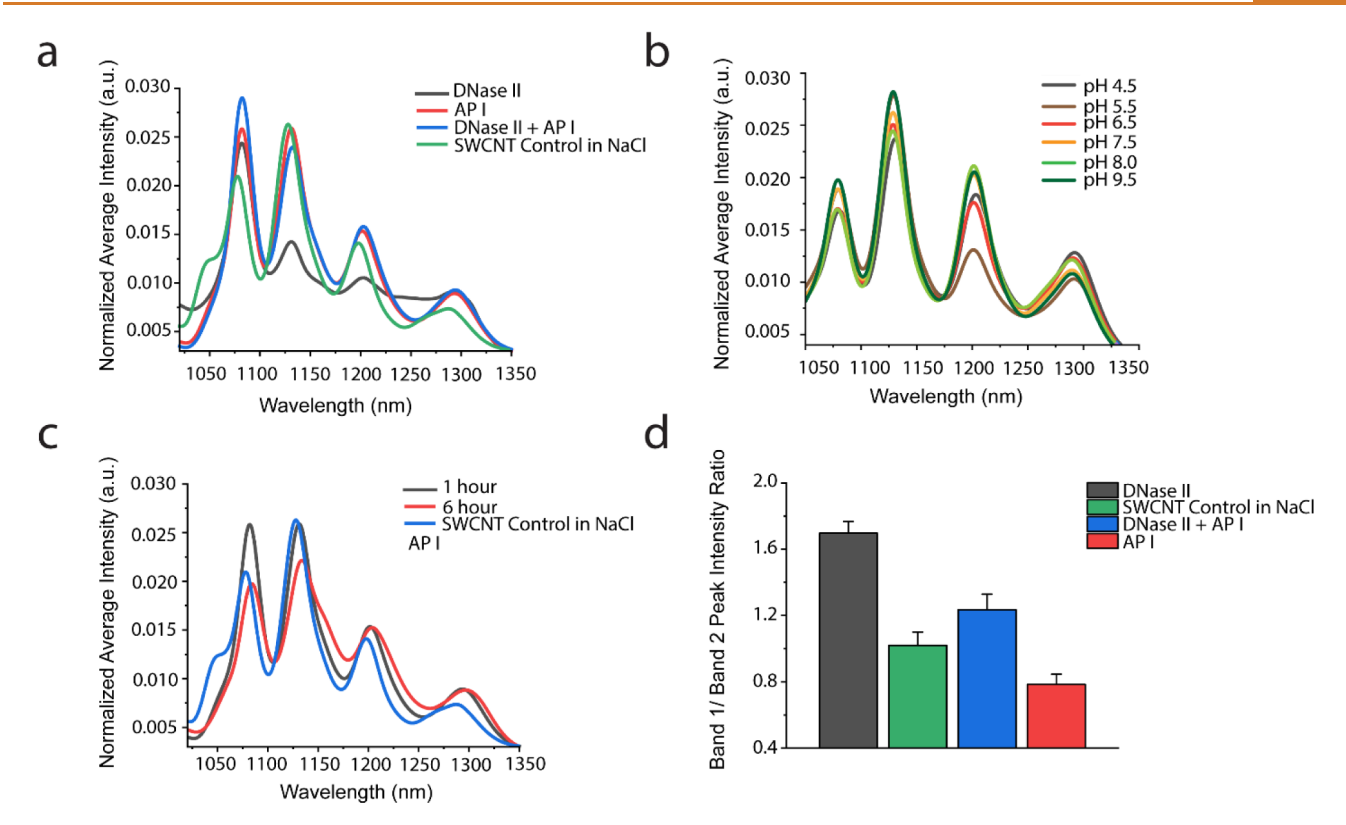


Figure 4. Solution phase experiments recapitulating the NIR fluorescence response of GT<sub>6</sub>-SWCNTs to the endolysosomal environment. (a) Spectral response to DNase-II and AP-1. (b) Spectral response to varying pH environments. (c) Time-dependent response to both DNase-II and AP-1. (d) Bar graph showing comparison of band peak intensity ratios for all phenotypes.

of unknown macrophage samples into either the M1, M2, or NM cell category. We selected the support vector machine (SVM) as the ML model for this purpose. SVM is a supervised learning algorithm designed for solving complex classification, regression, and outlier detection problems. It achieves this by performing optimal data transformations that delineate boundaries between data points based on predefined class labels or outputs. SVM modeling has proven effective in various applications and has recently gained momentum within healthcare and medicine. Alzheimer and selection of various diseases such as diabetes, Alzheimer's, psoriasis, hepatitis, hepatitis, and more.

Utilizing this SVM ML model, we examined the ability of DNA-SWCNTs to identify differing cell phenotypes as a function of DNA length. In Figure 5a, one identifiable feature, i.e., band 1 center wavelength, is shown as a function of DNA length and macrophage phenotype. Upon statistical analysis, DNA-SWCNTs composed of the shortest DNA sequence, i.e., the GT6, exhibited the largest statistically significant modulations. We speculate that this is due to the relative instability and mobility of shorter DNA strands on the SWCNT surface. 19 Similarly, GT<sub>6</sub>-SWCNTs can achieve higher chirality-dependent fluorescence modulation due to the increased degree of ease for the removal of DNA from the nanotube surface through adsorption of other amphiphilic molecules.<sup>19</sup> Another credible explanation can also be the increased interaction between the phosphate backbone of DNA and charged species in the surroundings that can easily induce confirmational changes, thus achieving a greater degree of modulation. Additional comparisons are found in Figures S24 and S25. With this DNA length-dependence in mind, we

trained individual SVM models based on NIR fluorescence spectra of DNA-SWCNTs within macrophages of known phenotype. For GT<sub>6</sub>-SWCNTs, although 101 predictors were input into the model, a principal component analysis and feature importance score sorting using an ANOVA analysis were performed (Figure S26) and only 42 significant predictors explaining at least a 95% variance were selected. Figure 5b shows a bar graph demonstrating that for both validation and test data; GT<sub>6</sub>-SWCNTs achieved the highest accuracy at about 87%. GT<sub>15</sub> exhibited moderate accuracy, reaching approximately 59%, while GT<sub>30</sub> significantly underperformed with an accuracy of only 19%. The SVM ML accuracies were also determined as a function of time point (Figure 5c). All models trained with GT<sub>6</sub> data consistently achieved accuracies greater than 87%. Notably, three of the GT<sub>6</sub> models surpassed 90% accuracy, and the model trained with data from the 6 h time point exhibited the highest accuracy at approximately 95%. When delineated by cell phenotype, the model demonstrates the highest accuracy for predicting M1 and M2 macrophages, with 98% and 96% accuracies, respectively, as shown in Figure 5d. The accuracy for NM cells was comparatively lower at roughly 78%. The lower accuracy of NM cells is attributed to a significant overlap of principal component analysis features between M2 and naive macrophages, as depicted in Figure 4e. Figure 4f shows a receiver operating curve (ROC), further affirming the high predictive power of the model. The ROC curve is a valuable tool for assessing the trade-off between sensitivity and specificity in classification models. A classification error plot shown in Figure S27 was made to check the model for errors, discrepancies, and optimize hyperparameters for accuracy.

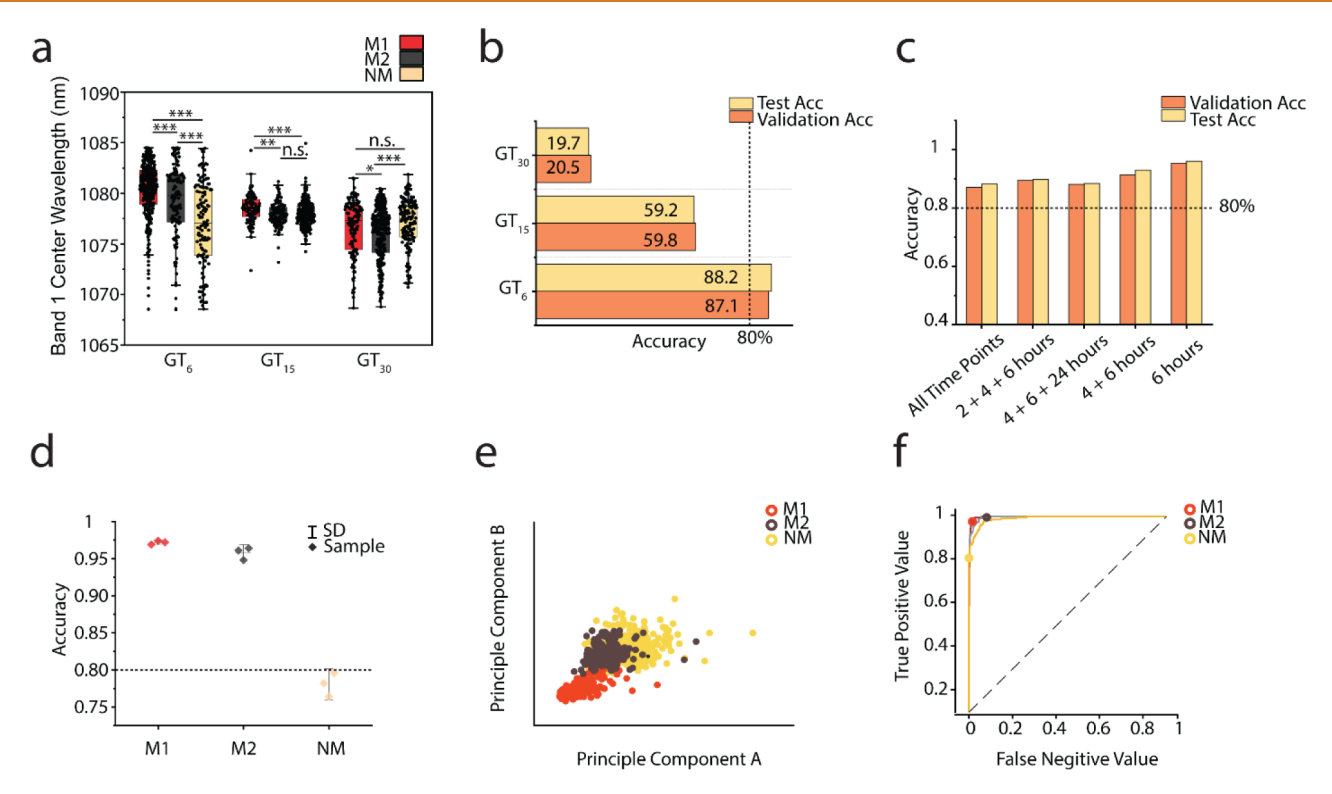


Figure 5. Machine learning for phenotype identification. (a) Band 1 center wavelength feature comparison between three different DNA-SWCNTs, i.e.,  $GT_{6}$ ,  $GT_{15}$ , and  $GT_{30}$ . Minimum of  $n \ge 300$  cells per condition were used. Boxes represent 25-75% of the data, horizontal lines represent medians, and whiskers represent mean  $\pm$  s.d. A two-sample t test hypothesis testing analysis was performed (\*\*\*p < 0.001, \*\*p < 0.01, and \*p < 0.05). (b) Bar graph indicating accuracy of test and validation data for all tested DNA-SWCNTs. (c) Bar graph indicating accuracy of test and trained data for  $GT_{6}$ -SWCNT evaluated for different time point data sets. (d) Interval plot indicating accuracy of predicting each macrophage phenotype. (e) Principal component A and B cluster plots showing each cell type cluster. (f) ROC curve for each macrophage phenotype indicating true positive and false negative values.

The higher predictive accuracy, especially for M1 and M2 macrophages, and the corresponding ROC curve, contribute to the overall confidence in the robustness and reliability of the GT<sub>6</sub> SVM model for identifying and distinguishing between different macrophage phenotypes. Furthermore, these results also underline the consistency of the GT<sub>6</sub>-SWCNT model across various time points with particularly high accuracy rates observed. The superior performance of the model trained with data from the 6-hour time point suggests that this specific time point provides highly discriminatory features for accurately identifying cell phenotypes. It is imperative to note that number of data points to train data were kept constant to avoid any issues arising from over- or under-fitting of data. It is also important to note that previous studies have shown this 6-hour time scale is very significant for intracellular studies. Machine learning data for other time points can be found in Figures S28 and S29. Overall, the findings emphasize the potential of GT<sub>6</sub>-SWCNT data in developing accurate and reliable machine learning models for cell phenotype identification.

For future *in vivo* applications of the spectral fingerprinting approach, we demonstrate feasibility with the use of a custombuilt NIR probe spectrophotometer.<sup>73</sup> A schematic of the probe spectrophotometer is shown in Figure 6a. The setup incorporates a 730 nm laser passing through a two-way fiber optic cable and illuminating a Petri dish of M1, M2, or NM cells containing DNA-SWCNTs. The fluorescence emission is directed back into the fiber optic probe, which routes it into a spectrometer connected to a 1D InGaAs detector, providing an output in the form of an NIR spectrum. Figure 6b,c represent

the normalized output from the probe spectrophotometer at 0.5 and 2 h after a 30 min incubation with 5 mg L<sup>-1</sup> GT<sub>6</sub>-SWCNTs. Evident intensity changes between the two band species can be observed. Figure 6d shows the differential peak intensity ratio comparisons for all phenotypes at 0.5 h post SWCNT dose. Significant differences in intensity ratios observed are features that can easily enable the identification of macrophage phenotypes with considerable accuracy. This approach holds promise for application *in vivo* wound models, such as live mice, enabling real-time monitoring of macrophage subtype population. Moreover, in the future, it can also serve as a valuable tool in medical research for tracking stem cell differentiation *in vivo*. Further advancements and research may also position it as a diagnostic assay for early cancer detection.

To evaluate the use of DNA-SWCNT-based cell phenotyping in a more clinically relevant application, i.e., in primary cells, the same type of NIR spectral analysis was performed with bone marrow-derived macrophages (BMDMs) isolated using bone marrow from femoral and tibial bones of eight- to ten-week-old mice. Figures 7a and S30 visual representations of all the cell phenotypes and clearly show the apparent differences in NIR brightness among all three cell types. Interestingly, like previous figures, significant band center wavelength and intensity modulations are observed among M1, M2, and naive BMDM samples through time, as shown by Figure 7b,c. Similarly, a closer look at these features indicates statistically significant differences in the band peak intensity ratios when comparing all three cell phenotypes, as shown in Figure 7d. More distinguishable NIR features as well as the

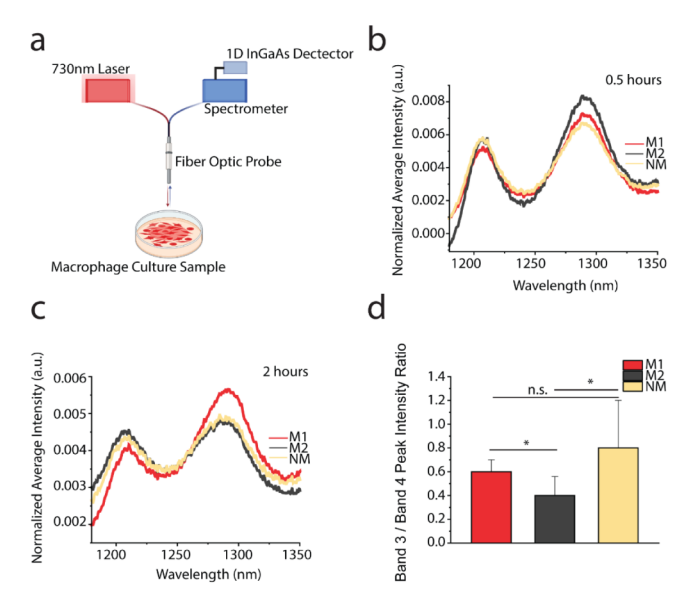


Figure 6. Measurements for future in vivo applicability of the spectral fingerprinting approach. (a) A schematic diagram showing the fiber optic NIR probe spectrometer setup for sample data collection. (b)  $GT_6$ -SWCNT sensor probe response at 0.5 h. (c)  $GT_6$ -SWCNT sensor probe response at 2 h. (d) Bar graph showing the comparison of band peak intensity ratios for all phenotypes. Bars represent the average and whiskers represent mean  $\pm$  s.d. for each condition ( $n \ge 5 \times 10^5$  cell per mL per Petri dish). A two-sample t test hypothesis testing analysis was performed between different samples and between different time points (\*p < 0.05).

SVM confusion matrix for primary macrophages can be found in Figures S31 and S32. Together, these distinct differences demonstrate the applicability of our sensor platform toward *in vivo* applications, offering the potential for real-time monitoring and analysis of cellular responses and comparison of different cell phenotypes present within living organisms.

To quantify potential deleterious effects on cell health as a function of polarization state and DNA-SWCNT concentration, two distinct methods, xCELLigence and annexin V/PI assays, were employed to assess the response of each cell phenotype. The first method involved real-time monitoring of cell proliferation using an xCELLigence Real-Time Cell Analysis system. This system measures electrical impedance across integrated microelectrodes embedded in the bottom of specialized 16-well tissue culture E-plates. The impedance measurement is represented as a cell index value, which can be directly correlated to various cellular characteristics, including cell growth, viability, adhesion, activity, and morphology. Figure 8a illustrates the normalized cell index of RAW 264.7 NM cells dosed with 0.1, 1, or 10 mg  $L^{-1}$  GT<sub>6</sub>-SWCNTs. The data reveal that the highest cell proliferation occurred at a DNA-SWCNT dose of 1 mg L<sup>-1</sup>, while a dose of 10 mg L<sup>-1</sup> considerably decreased the cell viability. Interestingly, higher DNA-SWCNT concentrations resulted in greater rates of cell proliferation, activity, and viability of M1 macrophages, with 10 mg L<sup>-1</sup> showing the highest response (Figure 8b). The response of M2 macrophages mirrors that of NM cells with maximum growth and proliferation observed at a dose of 1 mg  $L^{-1}$  and a minimum growth rate observed at 10 mg  $L^{-1}$  (Figure

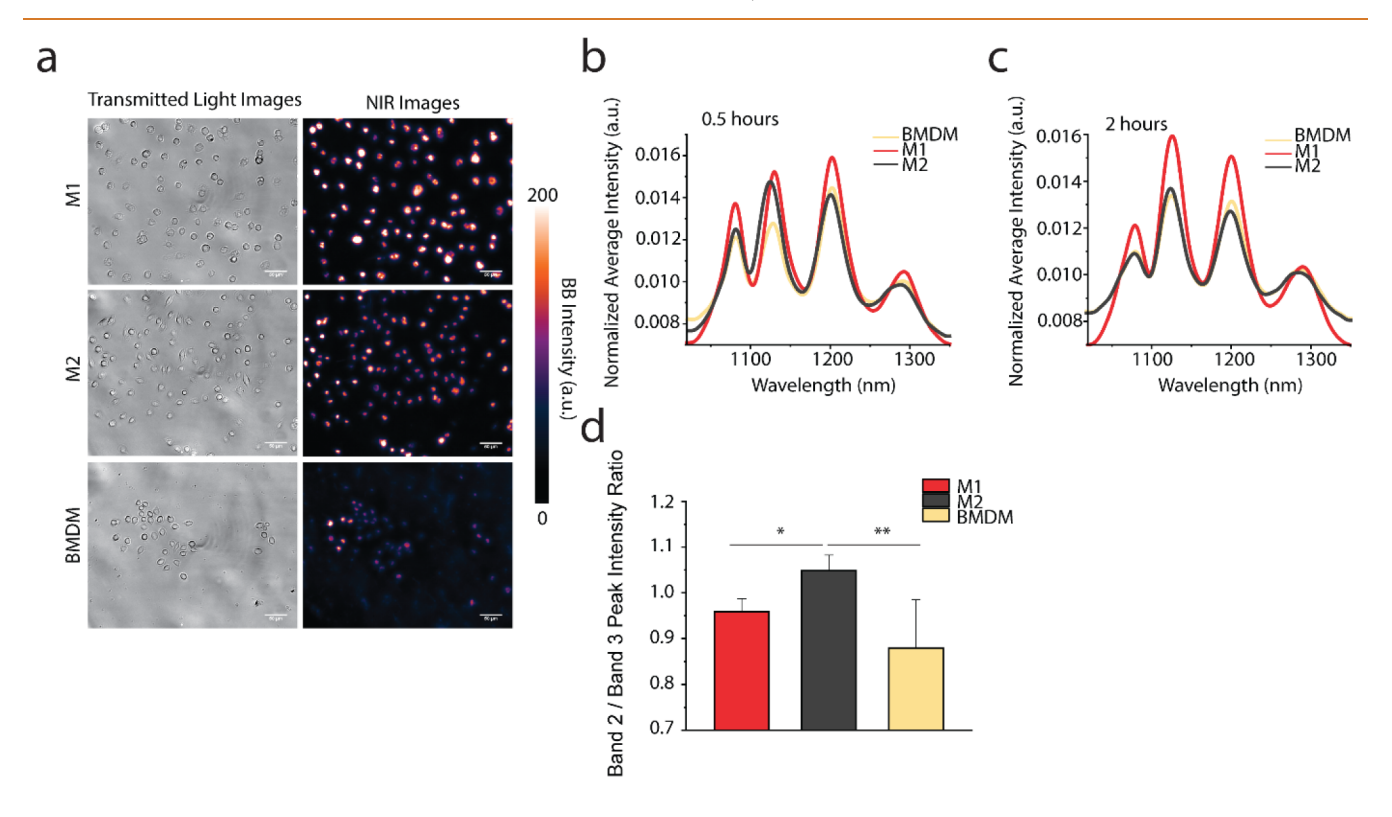


Figure 7. Simulating applicability of the spectral fingerprinting approach in primary BMDM cells. (a) Transmitted light and NIR fluorescence images for all cell types M1, M2, and naive BMDM at 0.5 h. (b) Normalized average intensity for all cell phenotypes at 0.5 h. (c) Normalized average intensity for all cell phenotypes at 2 h. (d) Bar graph showing comparison of band peak intensity ratios for all phenotypes. Bars represent the average and whiskers represent mean  $\pm$  standard deviation for each condition ( $n \ge 300$ ). A two-sample t test hypothesis testing analysis was performed between different samples and between different time points (\*\*p < 0.01 and \*p < 0.05).

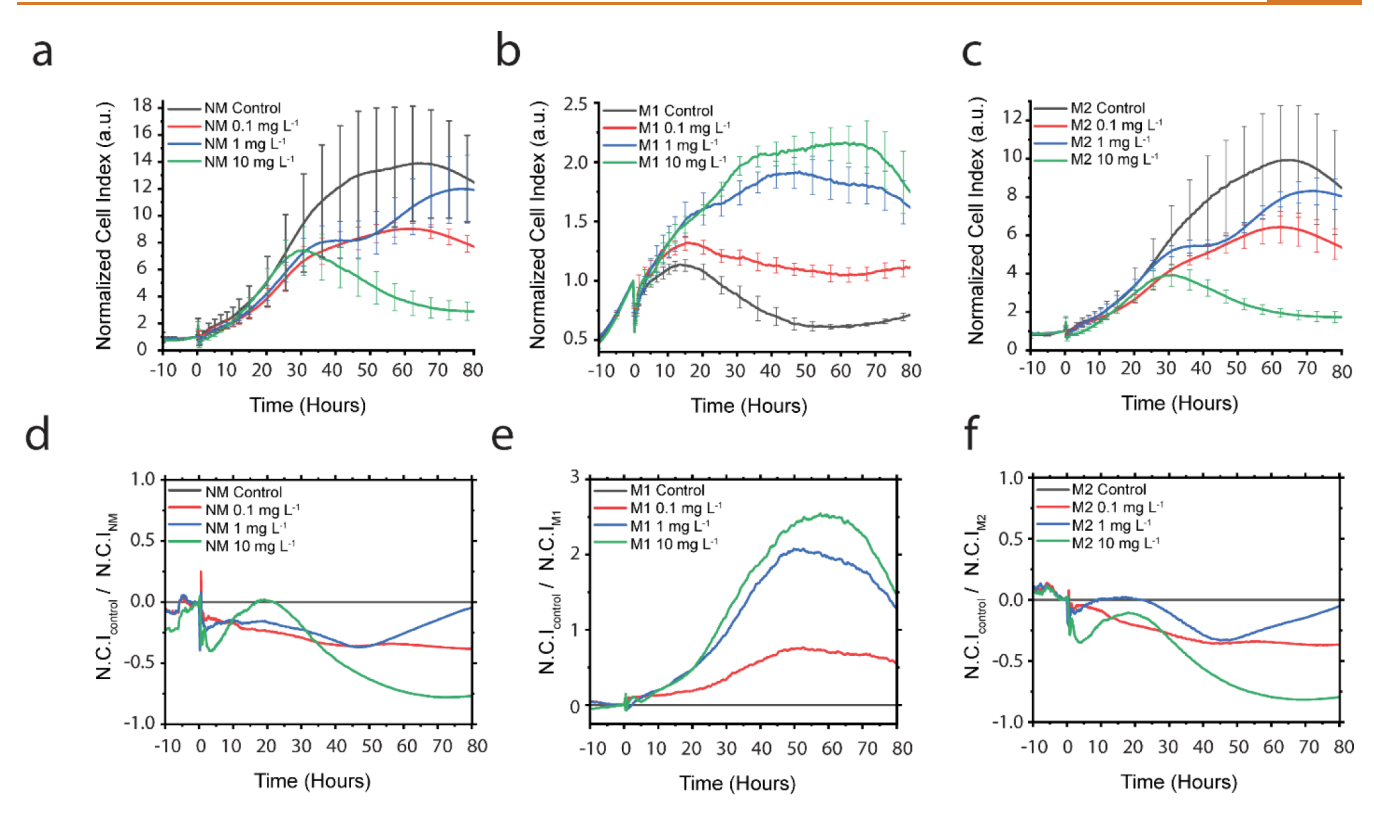


Figure 8. Real-time cell proliferation and cytotoxicity of RAW 264.7 macrophages exposed to DNA-SWCNTs. Cell proliferation curves for (a) naive macrophages, (b) M1 macrophages, and (c) M2 macrophages over a continuous period of 3 days. Cell index normalized to the no-SWCNT control cell index for (d) naive macrophages, (e) M1 macrophages, and (f) M2 macrophages as a relative measure of cell activity.

ı

By normalizing the cell index of each macrophage phenotype to the cell index of its respective control, a measure for relative cellular activity over time was determined (Figure 8d-f). Both M2 and NM cells exhibit an identical response with their activity lower than that of their respective controls. Upon closer examination of M1 macrophages, it is observed that all M1 macrophages dosed with DNA-SWCNT outperformed the control in terms of cellular activity, with the highest nanotube dose demonstrating the highest activity. The enhanced activity of M1 macrophages is attributed to their higher uptake of DNA-SWCNTs. We speculate, due to their pro-inflammatory nature, M1 macrophages tend to proliferate more when internalizing more DNA-SWCNTs. This observation suggests that the presence of a higher concentration of SWCNTs may stimulate the activity and growth of M1 macrophages, providing valuable insights into the complex interplay between nanomaterials and immune cell responses.

A second method for monitoring cell health was an apoptosis-necrosis assay, performed to investigate the effects of DNA-SWCNT concentration on different macrophage phenotypes, as shown in Figure S33. Results did not show any major cell necrosis in any samples except M1 cells. This was attributed to scraping the M1 cells from the Petri dish surface, which has been discussed in Figure S33.

# **CONCLUSION**

Figure 9 represents a simplified schematic for the process used to identify macrophage phenotypes using single-walled carbon nanotube near-infrared spectral fingerprinting. In conclusion, this comprehensive study employs a multifaceted approach to unravel the intricate interactions between distinct macrophage phenotypes and DNA-SWCNTs. A crucial finding highlights

the paramount importance of selecting an appropriate DNA sequence length for accurate cell phenotype identification based on NIR fluorescence data, with an emphasis on efficacy of shorter sequences. Moreover, the study affirms the potency of SWCNT-based spectral fingerprinting, particularly when coupled with machine learning, as an invaluable tool for precisely categorizing cellular states based on complex spectral data. This innovative approach holds great promise in advancing our understanding of dynamic cellular processes, disease states, disease progression, and response to stimuli in vivo. The platform's sensitivity to minute changes in the NIR spectrum positions it as a valuable tool for researchers and clinicians. It facilitates the real-time monitoring of cellular behavior within living systems, offering insights that extend to both fundamental research and clinical applications. The implications of this research provide a significant contribution for future developments in nanotechnology and biomedicine, bridging the gap between spectral analysis and cellular dynamics for enhanced diagnostic and therapeutic interventions.

#### **METHODS AND MATERIALS**

**DNA-SWCNT Sample Preparation.** To create monodispersed ssDNA-wrapped SWCNTs (ssDNA-SWCNTs), 1 mg of as-synthesized SWCNT powder was added to 2 mg of (GT)<sub>xx</sub> oligonucleotide (Integrated DNA Technologies) and 1 mL of 0.1 M NaCl (Sigma-Aldrich). Each sample was ultrasonicated using a 1/8" tapered microtip for 30 min at 40% amplitude in an ice bath (Sonics Vibracell VCX-130; Sonics and Materials). The resulting suspensions were ultracentrifuged (Beckman Optima MAX-XP) for 30 min at

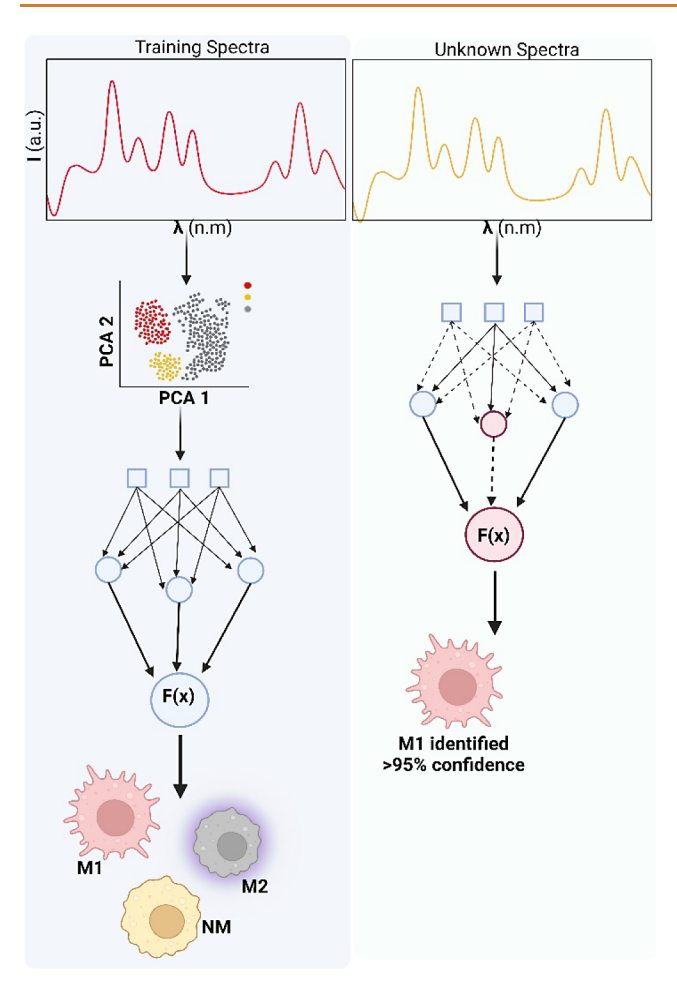


Figure 9. Conclusion schematic. A simplified schematic for the accurate identification of immune cell phenotypes using a support vector machine learning model.

250,000 g and 4 °C, and the top ~80% of the supernatant was collected.

Near-Infrared Fluorescence Microscopy. A hyperspectral NIR fluorescence microscope, similar to a previously detailed system, was used to obtain all hyperspectral fluorescence data. A 660 nm excitation laser source was reflected onto the sample stage of an Olympus IX-73 inverted microscope equipped with a LCPlan N,  $20\times/0.45$  IR objective by Olympus, U.S.A. The resulting fluorescence emission was passed through a volume Bragg grating and collected with a 2D InGaAs array detector by Photon Etc., (Montreal, Canada) to generate spectral image stacks. Live cell samples were mounted on a stage top incubator by Okolab, to maintain 37 °C and 5%  $CO_2$  cell culture conditions throughout the imaging procedure. All hyperspectral cubes, fluorescence images, and transmitted light images were background corrected and processed in MATLAB.

**Confocal Raman Microscopy.** All Raman data was acquired using an inverted WiTec Alpha300R confocal Raman microscope (WiTec, Germany) equipped with a Zeiss Epiplan-NEOFLUAR 100×/1.3 Oil Pol, oil immersion, objective, a 785 nm laser (20 mW output measured at the sample), and a UHTS 300 spectrograph (300 lines/mm grating) coupled with an Andor DR32400 CCD detector (-61C, 1650 pixels × 200 pixels). Singular cell areas were scanned, and spectra were obtained in 1 × 1 um intervals using

a 0.2s integration time per spectrum to construct hyperspectral images of individual cells. Background subtraction and cosmic ray removal were performed using a polynomial function in WiTec Project 5.2 software. Hyperspectral data was extracted and processed using custom codes written with MATLAB for integrated G-band, D-band, and  $I_{\rm D}/I_{\rm G}$  values.

**Cell Culture.** RAW 264.7 TIB-71 cell line from ATCC (Manassas, VA, USA) was cultured under standard incubation conditions at 37 °C and 5% CO2. "D-10" cell culture media containing sterile filtered high-glucose DMEM with 10% heat inactivated FBS, 2.5% HEPES, 1% L-glutamine, 1% penicillin/streptomycin, and 0.2% amphotericin B (all from Gibco) was used for cell culture. 0.5 ng mL<sup>-1</sup> of cytokines and signaling molecules were added to media during each experiment to avoid cells losing their polarization states.

Sample Preparation for Optical Microscopy. For all 20× in vitro NIR fluorescence imaging experiments the cells were plated, in triplicate, at an initial concentration  $5.26 \times 10^4$ cells/cm<sup>2</sup> on 35 mm glass-bottom microwell dishes (MatTek) and allowed to culture overnight. To dose the cells with nanotube samples, the culture media was removed and replaced with 1 mg L<sup>-1</sup> of either purified-SWCNTs or unpurified-SWCNTs diluted in D10 cell culture media and incubated for 30 min to allow cell internalization. The SWCNT-containing media was then removed, the cells were washed twice with sterile PBS (Gibco) followed by the addition of fresh media. All time points were defined with respect to this step. For the 100× confocal Raman microscopy experiments, the same cell plating and SWCNT dosing procedures were followed as highlighted previously; however, the cells were fixed with paraformaldehyde (Electron Microscopy Sciences). Cell fixation was performed with 4% PFA in PBS for 15 min, after which the cells were rinsed three times and covered with PBS to retain an aqueous environment during imaging.

Cell Viability Assay. RAW 264.7 macrophage cells were plated on 35 mm glass-bottom microwell dishes (MatTek) and allowed to culture overnight (with cytokine dosed media) at an initial seeding density of  $5.26 \times 10^4$  cells per cm<sup>2</sup>. The following day, the medium was replaced with 1 mg L<sup>-1</sup> SWCNTs diluted in the medium and incubated for an additional 24 h. After 24 h, the cells were collected from the dishes and stained with annexin V and propidium iodide (Dead Cell Apoptosis Kit V13242, Invitrogen) following the manufacturer's protocol. Fluorescence images of the stained cells were acquired by using a Cellometer Vision CBA image cytometer (Nexcelom Bioscience), and images were analyzed by using ImageJ and custom MATLAB codes, which background subtracted and integrated fluorescence from whole fields of cells. For each cell condition, a control dish was plated without SWCNT addition to create the gates on the annexin V and propidium iodide axes of the histograms.

**Bone Marrow Cell Isolation.** To generate BMDMs, the femoral and tibial bones of 8–10-week-old mice were flushed with RPMI media (Thermo Fisher) and the bone marrow suspension was passed through a 70 μm cell strainer. Bone marrow cells were cultured in T75 nontissue-culture flasks with 10 mL of RPMI medium (Thermo Fisher) supplemented with 10% heat-inactivated fetal bovine serum, 2 mM L-glutamine, 25 mM HEPES, and 20% L929 conditioned medium and kept in a humidified incubator at 37 °C with 5% CO<sub>2</sub>. An additional 5 mL of media was added to plates on day 3 of differentiation. After 7–10 days of differentiation, the loosely adherent cells

were harvested by gentle washing with 2 mM EDTA (Thermo Fisher) in PBS (Thermo Fisher), cells were seeded in 12-well plates at a density of  $3 \times 10^5$  per mL, were pooled and used as the starting source of cells for most experiments. BMDMs were seeded overnight in 12-well plates (2.5 ×  $10^6$  per well; 1 mL culture medium before infection).

**Macrophage Differentiation.** To induce differentiation of macrophages into M1 and M2 phenotypes, a combination of signaling molecules were added. M1 were obtained by exposing the cells to a dose containing 0.5 ng mL<sup>-1</sup> of lipopolysaccharide (LPS) and interferon-gamma (IFN-γ). LPS, derived from the outer membrane of Gram-negative bacteria, and IFN- $\gamma$ , a pro-inflammatory cytokine, collectively drive cell polarization toward the M1 phenotype. Conversely, to obtain M2, a separate set of signaling molecules were used. A dose of 0.5 ng mL<sup>-1</sup> of interleukin-4 (IL-4) and interleukin-10 (IL-10) were introduced simultaneously. IL-4 and IL-10 cytokines are both associated with anti-inflammatory responses, which contribute equally to the polarization of macrophages toward the M2 phenotype. Cells were incubated with the cytokine mixtures overnight, for 24 h, to achieve maximum cell polarization and were later evaluated for characteristic differences among each cell phenotype, before proceeding with any experimentation.

Real-Time Near-Infrared Fluorescence Spectroscopy. Petri dishes were seeded with cells to achieve a density of 5 × 10<sup>5</sup> cells. Consequently, cells were dosed with respective cytokines to polarize them into M1 and M2 macrophages. After 24 h, 5 mg L<sup>-1</sup> of GT<sub>6</sub>-SWCNTs were added to cells, and after the 30 min incubation period, cells were washed with 1× PBS and replenished with fresh media. NIR fluorescence spectra were acquired from each sample at 0.5 and 2 h. Individual NIR fluorescence spectra from cell samples were obtained using a custom-built preclinical fiber optics probe spectroscopy system described in previous studies. A custom MATLAB code was used to perform background subtraction and post analysis on acquired fluorescence data.

Near-Infrared Fluorescence Spectroscopy for Lysosomal Solution Experiments. 10 ng mL $^{-1}$  of deoxyribonuclease II (DNase II), activating protein-1 (AP-1), and a mixture of both DNase-II and AP-1 was used as model biomolecules for lysosomal environments. Solutions of AP-1 and DNase-II were made in high purity Milli-Q water (at 37  $^{\circ}$ C) and incubated with 0.1 mg/L of SWCNTs. The mixture was vortexed and placed in the incubator at 37  $^{\circ}$ C for 15 min, and 160  $\mu$ L of each mixture was added to a 96 well-plate for imaging.

Macrophage Identification. To discern M1 macrophage characteristics, APC antimouse CD11c and FITC antimouse CD38 antibodies (BioLegend) were utilized. These antibodies were specifically employed for the precise detection of M1 macrophage markers, including CD38 and CD11c. These selected markers play a pivotal role in identifying distinctive characteristics associated with M1 macrophages using flow cytometry. Subsequently, M2 macrophages were also identified. In this regard, M2-specific markers, CD206 and CD163, were targeted for detection using PE/Dazzle 594 antimouse CD 206 (MMR) and APC antimouse CD163 antibodies (BioLegend). An Anti-CD16/CD32 Fc receptor blocking antibody was used to eliminate nonspecific receptor binding. This meticulous approach allowed for the comprehensive identification of M1 and M2 macrophage phenotypes post cytokine addition.

FACS Flow Cytometry. Cells were detached using TrypLE from Petri dishes and resuspended in cell staining buffer (PBS + 0.5–1% BSA) at a density of 5  $\times$  10<sup>6</sup> cells per mL. Staining was done at 4 °C. 100  $\mu$ L of cells were added to centrifuge tubes followed by 100  $\mu$ L of Fc blocking antibody (1:50 ratio in buffer). The cells were incubated for 20 min followed by centrifugation at 1500 rpm for 5 min at 4 °C. Supernatant was discarded, and the cells were further incubated for 30 min with marker specific antibodies (0.1  $\mu$ g mL  $^{-1}$ ) in 100  $\mu$ L of buffer in the dark. The cells were then washed by centrifuging at 1500 rpm for 5 min. Washing was repeated 3 times to remove any unbound markers. The cells were then resuspended in 200  $\mu$ L of FACS buffer for flow cytometry.

FACS Flow Cytometry Analysis. A BD FACSVerse Cell Analyzer was used to perform flow cytometry experiments. QA/QC was performed on the equipment before cell analysis to optimize detector voltage settings. BD FACSuite version 1.0.6 was used for data analysis and cell gating. Three different gating strategies were employed during the data analysis. Naive macrophages were used as a control to determine the gating quadrants. Forward and side scatter density plots were used to determine cell populations in the sample in the first pass. This was followed by forward height and scatter plots for doublet cell exclusion to avoid any false positive. Two parameter density plots were also used to confirm cell phenotypes depending on multiple fluorescent markers.

Label-Free Cell Proliferation and Adherence Monitoring. Adherence and proliferation were measured with an xCELLigence real-time cell analysis instrument from Agilent. For baseline impedance measurements of the wells, 140  $\mu$ L of cell media was added to each of the 16 wells in the E-plate. 50  $\mu L$  of cells diluted in media was added to each well to reach a final concentration of  $2 \times 10^5$  cells per well. The cells were allowed to adhere to the plates for 30 min in a cell culture hood to allow for an evenly distributed initial seeding of cells over the electrodes. After 30 min, the E-plates were placed into the xCELLigence system and data acquisition occurred every 15 min. Plates were incubated for 24 h. Subsequently, respective cytokines were added, and the cells were incubated for an additional 24 h to polarize macrophages into M1 or M2 phenotypes. The cells were then dosed with three different concentrations of GT<sub>6</sub>-SWCNTs: 0.1, 1, and 10 mg L<sup>-1</sup>, in separate wells.

**Data Collection for Machine Learning.** Near-infrared spectral data from 950 to 1350 nm was used to train the machine learning model. For each cell type and time point, both technical and biological replicates were acquired to confirm the reproducibility and repeatability of experiments. Each cell type had an estimated 50,500 data points per time point. Training data set for one time point was an estimated 1.5 million data points. Total training data set size for all time points was an estimated 6 million. A data point is termed the 101 recorded features in the near-infrared spectrum per cell.

Data Processing for Machine Learning. The ImageJ software was used to identify and mask single living cells as regions of interest using the ROI manager. The near-infrared spectral data coupled with ROI data from ImageJ was fed into a custom-made MATLAB graphical user interface (GUI) to segment data based on single cells analysis. The resulting data files were preprocessed and formatted using another custom-made MATLAB GUI to rearrange data for the MATLAB Classification Learner.

Machine Learning Optimization. The MATLAB classification learner from the machine learning and deep learning toolbox was used to train a support vector machine on the segmented data based on single cell analysis. 101 predictors were initially used for data prediction. 75% of the data was used for model training. Validation of the training data set was performed using MATLAB in-built hold-out validation method at a percentage of 25%. A completely separate set of test data was used to evaluate model performance after tuning, optimizing, and training the model to avoid problems with overfitting.

**Statistical Analysis.** OriginPro 2022b was used to perform all the statistical analyses. All data either met assumptions of statistical tests performed (i.e., equal variances, normality, etc.) or were transformed to meet assumptions before any statistical analysis was caried out. Statistical significance was analyzed using a two-sample *t* test or one way ANOVA where appropriate. Testing of multiple hypotheses was accounted for by performing one-way ANOVA with Tukey's posthoc test.

## **ASSOCIATED CONTENT**

# **5** Supporting Information

The Supporting Information is available free of charge at https://pubs.acs.org/doi/10.1021/acsnano.4c03387.

Additional figures of DNA-SWCNT optical characterization, intracellular data, fluorescence assisted flow cytometry data, ROI selection and analysis, Raman Gband and D-band maps, Raman spectra from DNA-SWCNTs in all cell phenotypes, annexin V/propidium iodide cell assay results, DNA-SWCNT near-infrared feature analysis, support vector machine confusion matrices, receiver operating curves, validation figures and error analysis figure, and a table with a list of near-infrared features trained use in machine learning (PDF)

#### **AUTHOR INFORMATION**

# **Corresponding Author**

Daniel Roxbury — Department of Chemical Engineering, University of Rhode Island, Kingston, Rhode Island 02881, United States; Email: roxbury@uri.edu

## Authors

Aceer Nadeem — Department of Chemical Engineering, University of Rhode Island, Kingston, Rhode Island 02881, United States; orcid.org/0000-0002-5381-3561

Sarah Lyons – Department of Chemical Engineering, University of Rhode Island, Kingston, Rhode Island 02881, United States

Aidan Kindopp — Department of Chemical Engineering, University of Rhode Island, Kingston, Rhode Island 02881, United States

Amanda Jamieson — Department of Molecular Microbiology and Immunology, Brown University, Providence, Rhode Island 02912, United States; orcid.org/0000-0002-5781-9231

Complete contact information is available at: https://pubs.acs.org/10.1021/acsnano.4c03387

#### Notes

The authors declare no competing financial interest.

#### **ACKNOWLEDGMENTS**

This work was supported by the National Science Foundation (CAREER Award #1844536 and #2231621) and the University of Rhode Island College of Engineering. A.J. was supported by the National Institutes of Health (R01HL165259-01A1 and R01HL126887). The confocal Raman data were acquired at the RI Consortium for Nanoscience and Nanotechnology, a URI College of Engineering core facility partially funded by the National Science Foundation EPSCoR, Cooperative Agreement #OIA-1655221. Research was made possible by the use of equipment available through the Rhode Island Institutional Development Award (IDeA) Network of Biomedical Research Excellence from the National Institute of General Medical Sciences of the National Institutes of Health under grant #P20GM103430 through the Centralized Research Core facility. TOC graphics and schematics were created using BioRender.com software.

#### REFERENCES

- (1) Horne, J.; McLoughlin, L.; Bridgers, B.; Wujcik, E. K. Recent developments in nanofiber-based sensors for disease detection, immunosensing, and monitoring. *Sens. Actuators Rep.* **2020**, *2*, 100005.
- (2) Wang, J.; et al. Peptide Nucleic Acid Probes for Sequence-Specific DNA Biosensors. J. Am. Chem. Soc. 1996, 118, 7667–7670.
- (3) Rocchitta, G.; et al. Enzyme Biosensors for Biomedical Applications: Strategies for Safeguarding Analytical Performances in Biological Fluids. *Sensors* **2016**, *16*, 780.
- (4) Pohanka, M. Overview of Piezoelectric Biosensors, Immunosensors and DNA Sensors and Their Applications. *Materials* **2018**, *11*, 448.
- (5) Borisov, S. M.; Wolfbeis, O. S. Optical Biosensors. *Chem. Rev.* **2008**, *108*, 423–461.
- (6) Mehrotra, P. Biosensors and their applications A review. J. Oral Biol. Craniofac. Res. 2016, 6, 153–159.
- (7) Shekhar, S.; Yadav, A. K.; Khosla, A.; Solanki, P. R. Review—Interleukins Profiling for Biosensing Applications: Possibilities and the Future of Disease Detection. *ECS Sens. Plus* **2022**, *1*, 041601.
- (8) Avouris, P.; Freitag, M.; Perebeinos, V. Carbon-nanotube photonics and optoelectronics. *Nat. Photonics* **2008**, *2*, 341–350.
- (9) John, P.; Vasa, N. J.; Zam, A. Optical Biosensors for the Diagnosis of COVID-19 and Other Viruses—A Review. *Diagnostics* **2023**, *13*, 2418.
- (10) Langer, A.; et al. A New Spectral Shift-Based Method to Characterize Molecular Interactions. *Assay Drug Dev. Technol.* **2022**, 20, 83–94.
- (11) Grasso, G.; et al. Fluorescent nano- and microparticles for sensing cellular microenvironment: Past, present and future applications. *Nanoscale Adv.* **2023**, *5*, 4311–4336.
- (12) Zavaleta, C.; et al. Noninvasive Raman Spectroscopy in Living Mice for Evaluation of Tumor Targeting with Carbon Nanotubes. *Nano Lett.* **2008**, *8*, 2800–2805.
- (13) Cherukuri, P.; Bachilo, S. M.; Litovsky, S. H.; Weisman, R. B. Near-Infrared Fluorescence Microscopy of Single-Walled Carbon Nanotubes in Phagocytic Cells. *J. Am. Chem. Soc* **2004**, *126*, 15638–15639
- (14) Lui, A.; Wang, J.; Chio, L.; Landry, M. P. Synthetic probe development for measuring single or few-cell activity and efflux. *Methods Enzymol.* **2019**, 628, 19–41.
- (15) Roxbury, D.; Jena, P. V.; Williams, R. M.; Enyedi, B.; Niethammer, P.; Marcet, S.; Verhaegen, M.; Blais-Ouellette, S.; Heller, D. A. Hyperspectral Microscopy of Near-Infrared Fluorescence Enables 17-Chirality Carbon Nanotube Imaging. *Sci. Rep.* **2015**, *5*, 14167.
- (16) Welsher, K.; Sherlock, S. P.; Dai, H. Deep-tissue anatomical imaging of mice using carbon nanotube fluorophores in the second

- near-infrared window. Proc. Natl. Acad. Sci. U. S. A. 2011, 108, 8943—8948.
- (17) Ackermann, J.; Metternich, J. T.; Herbertz, S.; Kruss, S. Biosensing with Fluorescent Carbon Nanotubes. *Angew. Chem., Int. Ed.* **2022**, *61* (18), No. e202112372.
- (18) Meran, M.; et al. Noncovalent Pyrene-Polyethylene Glycol Coatings of Carbon Nanotubes Achieve in Vitro Biocompatibility. *Langmuir* **2018**, *34*, 12071–12082.
- (19) Gravely, M.; Safaee, M. M.; Roxbury, D. Biomolecular Functionalization of a Nanomaterial To Control Stability and Retention within Live Cells. *Nano Lett.* **2019**, *19*, 6203–6212.
- (20) Mohan, H.; Bartkowski, M.; Giordani, S. Biocompatible Dispersants for Carbon Nanomaterials. *Appl. Sci.* **2021**, *11*, 10565.
- (21) Porter, A. E.; et al. Direct imaging of single-walled carbon nanotubes in cells. *Nat. Nanotechnol.* **2007**, *2*, 713–717.
- (22) Jena, P. V.; et al. A Carbon Nanotube Optical Reporter Maps Endolysosomal Lipid Flux. ACS Nano 2017, 11, 10689–10703.
- (23) Cao, Y.; et al. Enhanced Lysosomal Escape of pH-Responsive Polyethylenimine—Betaine Functionalized Carbon Nanotube for the Codelivery of Survivin Small Interfering RNA and Doxorubicin. ACS Appl. Mater. Interfaces 2019, 11, 9763—9776.
- (24) Holt, B. D.; Dahl, K. N.; Islam, M. F. Differential sub-cellular processing of single-wall carbon nanotubes via interfacial modifications. *J. Mater. Chem. B* **2015**, *3*, 6274–6284.
- (25) Delavary, B. M.; van der Veer, W. M.; van Egmond, M.; Niessen, F. B.; Beelen, R. H. J. Macrophages in skin injury and repair. *Immunobiology* **2011**, *216*, 753–762.
- (26) Italiani, P.; Boraschi, D. From Monocytes to M1/M2Macrophages: Phenotypical vs. Functional Differentiation. *Front. Immunol.* **2014**, *5*, 514.
- (27) Yunna, C.; Mengru, H.; Lei, W.; Weidong, C. Macrophage M1/M2 polarization. Eur. J. Pharmacol. 2020, 877, 173090.
- (28) Chen, S.; Saeed, A. F. U. H.; Liu, Q.; Jiang, Q.; Xu, H.; Xiao, G. G.; Rao, L.; Duo, Y. Macrophages in immunoregulation and therapeutics. *Signal Transduction Targeted Ther.* **2023**, *8*, 207.
- (29) Arango Duque, G.; Descoteaux, A. Macrophage Cytokines: Involvement in Immunity and Infectious Diseases. *Front. Immunol.* **2014**, *5*, 491.
- (30) Murray, P. J. Macrophage Polarization. Annu. Rev. Physiol. 2017, 79, 541-566.
- (31) Alisi, A.; et al. The Role of Tissue Macrophage-Mediated Inflammation on NAFLD Pathogenesis and Its Clinical Implications. *Mediators Inflammation* **2017**, 2017, 1–15.
- (32) Krzyszczyk, P.; Schloss, R.; Palmer, A.; Berthiaume, F. The Role of Macrophages in Acute and Chronic Wound Healing and Interventions to Promote Pro-wound Healing Phenotypes. *Front. Physiol.* **2018**, *9*, 419.
- (33) Chen, C.; Liu, T.; Tang, Y.; Luo, G.; Liang, G.; He, W. Epigenetic regulation of macrophage polarization in wound healing. *Burns Trauma* **2023**, *11*, tkac057.
- (34) Vogel, D. Y. S.; et al. Human macrophage polarization in vitro: Maturation and activation methods compared. *Immunobiology* **2014**, 219, 695–703.
- (35) Landén, N. X.; Li, D.; Ståhle, M. Transition from inflammation to proliferation: A critical step during wound healing. *Cell. Mol. Life Sci.* **2016**, *73*, 3861–3885.
- (36) Deng, X.; Gould, M.; Ali, M. A. A review of current advancements for wound healing: Biomaterial applications and medical devices. *J. Biomed. Mater. Res., Part B* **2022**, *110*, 2542–2573.
- (37) Isidro, R. A.; Appleyard, C. B. Colonic macrophage polarization in homeostasis, inflammation, and cancer. *Am. J. Physiol.: Gastrointest. Liver Physiol.* **2016**, 311, G59–G73.
- (38) Atri, C.; Guerfali, F.; Laouini, D. Role of Human Macrophage Polarization in Inflammation during Infectious Diseases. *Int. J. Mol. Sci.* **2018**, *19*, 1801.
- (39) Liu, Y.-C.; Zou, X.-B.; Chai, Y.-F.; Yao, Y.-M. Macrophage Polarization in Inflammatory Diseases. *Int. J. Biol. Sci.* **2014**, *10*, 520–529.

- (40) Liu, L.; Stokes, J. V.; Tan, W.; Pruett, S. B. An optimized flow cytometry panel for classifying macrophage polarization. *J. Immunol. Methods* **2022**, *511*, 113378.
- (41) Hickman, E.; et al. Expanded characterization of in vitro polarized M0, M1, and M2 human monocyte-derived macrophages: Bioenergetic and secreted mediator profiles. *PLoS One* **2023**, *18*, No. e0279037.
- (42) Kröger, M.; Scheffel, J.; Shirshin, E. A.; Schleusener, J.; Meinke, M. C.; Lademann, J.; Maurer, M.; Darvin, M. E.; et al. Label-free imaging of M1 and M2 macrophage phenotypes in the human dermis in vivo using two-photon excited FLIM. *Elife* **2022**, *11*, No. e72819.
- (43) Li, Y.; Liu, T.-M. Discovering Macrophage Functions Using In Vivo Optical Imaging Techniques. Front. Immunol. 2018, 9, 502.
- (44) Nordlohne, J.; Hulsmann, I.; Schwafertz, S.; Zgrajek, J.; Grundmann, M.; von Vietinghoff, S.; Eitner, F.; Becker, M. S. A flow cytometry approach reveals heterogeneity in conventional subsets of murine renal mononuclear phagocytes. *Sci. Rep.* **2021**, *11*, 13251.
- (45) Rostam, H. M.; Reynolds, P. M.; Alexander, M. R.; Gadegaard, N.; Ghaemmaghami, A. M. Image based Machine Learning for identification of macrophage subsets. *Sci. Rep.* **2017**, *7*, 3521.
- (46) Drescher, H.; Weiskirchen, S.; Weiskirchen, R. Flow Cytometry: A Blessing and a Curse. *Biomedicines* **2021**, *9*, 1613.
- (47) Chen, W.; Sandoval, H.; Kubiak, J. Z.; Li, X. C.; Ghobrial, R. M.; Kloc, M. The phenotype of peritoneal mouse macrophages depends on the mitochondria and ATP/ADP homeostasis. *Cell. Immunol.* **2018**, 324, 1–7.
- (48) Sicherre, E.; Favier, A.-L.; Riccobono, D.; Nikovics, K. Non-Specific Binding, a Limitation of the Immunofluorescence Method to Study Macrophages In Situ. *Genes* **2021**, *12*, 649.
- (49) Im, K.; Mareninov, S.; Fernando Palma Diaz, M.; Yong, W. H. An Introduction to Performing Immunofluorescence Staining Springer 2019, 299311, DOI: .
- (50) Hourani, T.; Perez-Gonzalez, A.; Khoshmanesh, K.; Luwor, R.; Achuthan, A. A.; Baratchi, S.; O'Brien-Simpson, N. M.; Al-Hourani, A. Label-free macrophage phenotype classification using machine learning methods. *Sci. Rep.* **2023**, *13*, 5202.
- (51) Gravely, M.; Roxbury, D. Multispectral Fingerprinting Resolves Dynamics of Nanomaterial Trafficking in Primary Endothelial Cells. *ACS Nano* **2021**, *15*, 12388–12404.
- (52) Jorio, A.; Saito, R. Raman spectroscopy for carbon nanotube applications. J. Appl. Phys. 2021, 129 (2), 021102.
- (53) Dillon, A. C.; et al. Systematic inclusion of defects in pure carbon single-wall nanotubes and their effect on the Raman D-band. *Chem. Phys. Lett.* **2005**, *401*, 522–528.
- (54) Dillon, A. C.; Yudasaka, M.; Dresselhaus, M. S. Employing Raman Spectroscopy to Qualitatively Evaluate the Purity of Carbon Single-Wall Nanotube Materials. *J. Nanosci. Nanotechnol.* **2004**, *4*, 691–703.
- (55) Nadeem, A.; et al. Enhancing Intracellular Optical Performance and Stability of Engineered Nanomaterials via Aqueous Two-Phase Purification. *Nano Lett.* **2023**, 23, 6588–6595.
- (56) Canton, J.; Khezri, R.; Glogauer, M.; Grinstein, S. Contrasting phagosome pH regulation and maturation in human M1 and M2 macrophages. *Mol. Biol. Cell* **2014**, 25, 3330–3341.
- (57) Tarique, A. A.; et al. Phenotypic, Functional, and Plasticity Features of Classical and Alternatively Activated Human Macrophages. *Am. J. Respir. Cell Mol. Biol.* **2015**, *53*, 676–688.
- (58) Pérez, S.; Rius-Pérez, S. Macrophage Polarization and Reprogramming in Acute Inflammation: A Redox Perspective. *Antioxidants* **2022**, *11*, 1394.
- (59) Lu, C.-H.; Lai, C.-Y.; Yeh, D.-W.; Liu, Y.-L.; Su, Y.-W.; Hsu, L.-C.; Chang, C.-H.; Catherine Jin, S.-L.; Chuang, T.-H. Involvement of M1Macrophage Polarization in Endosomal Toll-Like Receptors Activated Psoriatic Inflammation. *Mediators Inflammation* **2018**, 2018, 3523642.
- (60) Gravely, M.; et al. Aggregation Reduces Subcellular Localization and Cytotoxicity of Single-Walled Carbon Nanotubes. ACS Appl. Mater. Interfaces 2022, 14, 19168–19177.

- (61) Marneni, D.; Vemula, S. Analysis of COVID-19 using machine learning techniques. In *Statistical Modeling in Machine Learning*; Elsevier, 2023; pp. 3753, DOI: .
- (62) Varoquaux, G.; Cheplygina, V. Machine learning for medical imaging: Methodological failures and recommendations for the future. NPJ. Digital Med. 2022, 5, 48.
- (63) Lo, C.-S.; Wang, C.-M. Support vector machine for breast MR image classification. *Comput. Math. Appl.* **2012**, *64*, 1153–1162.
- (64) Gaonkar, B.; Shinohara, R. T.; Davatzikos, C. Interpreting support vector machine models for multivariate group wise analysis in neuroimaging. *Med. Image Anal.* **2015**, *24*, 190–204.
- (65) Sonawane, C.; Somwanshi, K.; Patil, R.; Raut, R. Diabetic Prediction Using Machine Algorithm SVM and Decision Tree; In 2023 International Conference on Applied Intelligence and Sustainable Computing (ICAISC), IEEE, 2023, 17, .
- (66) Sharma, A.; et al. Alzheimer's patients detection using support vector machine (SVM) with quantitative analysis. *Neurosci. Inform.* **2021**, *1*, 100012.
- (67) Vichianin, Y.; Khummongkol, A.; Chiewvit, P.; Raksthaput, A.; Chaichanettee, S.; Aoonkaew, N.; Senanarong, V. Accuracy of Support-Vector Machines for Diagnosis of Alzheimer's Disease, Using Volume of Brain Obtained by Structural MRI at Siriraj Hospital. *Front. Neurol.* **2021**, *12*, 640696.
- (68) Thamizhvani, T.; Ajayan, A. K.; Sannidhya, V.; Hemalatha, R.; Chandrasekaran, R. Psoriasis Skin Disease Identification Using Support Vector Machine(SVM) Image Classification and Determining the Growth Rate. *J. Phys.: Conf. Ser.* **2022**, *2318*, 012034.
- (69) Sartakhti, J. S.; Zangooei, M. H.; Mozafari, K. Hepatitis disease diagnosis using a novel hybrid method based on support vector machine and simulated annealing (SVM-SA). *Comput. Methods Programs Biomed.* **2012**, *108*, 570–579.
- (70) Alty, S. R.; Millasseau, S. C.; Chowienczyk, P. J.; Jakobsson, A. Cardiovascular disease prediction using support vector machines; In 46th Midwest Symposium on Circuits and Systems, IEEE, 2003, 376379, DOI: .
- (71) Elsedimy, E. I.; AboHashish, S. M. M.; Algarni, F. New cardiovascular disease prediction approach using support vector machine and quantum-behaved particle swarm optimization. *Multimed. Tools Appl.* **2024**, *83*, 23901–23928.
- (72) Harvey, J. D.; Zerze, G. H.; Tully, K. M.; Mittal, J.; Heller, D. A. Electrostatic Screening Modulates Analyte Binding and Emission of Carbon Nanotubes. *J. Phys. Chem. C* **2018**, *122*, 10592–10599.
- (73) Safaee, M. M.; Gravely, M.; Roxbury, D. A Wearable Optical Microfibrous Biomaterial with Encapsulated Nanosensors Enables Wireless Monitoring of Oxidative Stress. *Adv. Funct. Mater.* **2021**, *31*, 2006254.
- (74) Martinez-Serra, J.; et al. xCELLigence system for real-time label-free monitoring of growth and viability of cell lines from hematological malignancies. *OncoTargets Ther.* **2014**, *985*, *985*.
- (75) Roxbury, D.; Jena, P. V.; Shamay, Y.; Horoszko, C. P.; Heller, D. A. Cell Membrane Proteins Modulate the Carbon Nanotube Optical Bandgap *via* Surface Charge Accumulation. *ACS Nano* **2016**, 10, 499–506.